



Experimental and simulative investigation of an energy-autarkic, temperature field-based Sensor-integrating Plain Bearing focusing transient operating conditions

Thao Baszenski¹ · Johannes Groß¹ · Karl-Heinz Kratz² · Janek Paeßens² · Georg Jacobs¹ · Tobias Gemmeke² · Benjamin Lehmann¹ · Math Lucassen¹

Received: 31 March 2025 / Accepted: 5 September 2025
© The Author(s) 2025

Abstract

Increased usage of hydrodynamic plain bearings is being encountered in applications that require traversing the mixed friction area, such as in wind turbines gearboxes or heavy-duty drivetrains. These operating conditions are not covered by the established design standards. Condition monitoring systems (CMS) can detect such critical operating conditions—e.g. start-up procedures—and enable timely, condition-based maintenance to prevent damage.

In hydrodynamic plain bearings, the lubrication gap height and the bearing temperature are key parameters for detecting failure-critical conditions. The research project “Auto-informative Plain Bearings” uses temperature field monitoring to detect critical conditions. Previous work showed that Gümbel-curve’s relation to the temperature field allows the lubrication gap height determination in fluid friction. In this work it will be proven that the developed CMS approach allows online detection of mixed friction. This paper outlines the CMS design process, focusing on testing under transient conditions and lubricant failure. Consequently, the CMS’s ability to identify critical events will be verified.

Sensor-integrating Machine Elements (SiME) need to fulfill the characteristic of energy autarky. The energy harvestable in thermal equilibrium by utilizing the waste heat using a plain bearing integrated thermogenerator (TEG) is determined. The harvestable energy budget is in the range of the non-optimized demand of the Sensor-integrating Plain Bearing (SiPB)-prototype. Finally, measures are derived to achieve permanent autarkic operation of the SiPB.

1 Introduction

Hydrodynamic plain bearings are increasingly being used in new applications that are not covered by the established design standards. Prominent examples are planetary plain bearings in wind turbines gearboxes [1] or plain bearings in start-stop systems of automobiles with automatic start-stop systems [2]. These new areas of application, which are not covered by standards, increase the risk of bearing damage during operation. In hydrodynamic plain bearings abrasive and adhesive wear are the cause of the majority of failures [3]. In the case of adhesive failure, damage pro-

gresses rapidly, leaving very limited time to initiate condition-based maintenance measures to avert the damage. The information provided by condition monitoring systems (CMS) can be used to control these non-standardized operating conditions by the implementation of maintenance actions. The successful application of maintenance measures allows downtimes to be minimized and costs to be saved.

Plain bearings are used, for example, in applications such as planetary gears in wind turbines. On the one hand, access to the machine element is difficult once the gearbox has been installed. On the other hand, the multi-axis rotating system complicates the wire routing for data and power transmission to the CMS. The concept of Sensor-integrating Machine Elements enables the development of autarkic and compact sensor nodes in such hard-to-reach applications. However, most established monitoring methods for plain bearings are not suitable for creating a SiME. The sensors either measure outside the plain bearing or require complex data evaluation with high energy demands. Estab-

✉ Thao Baszenski
thao.baszenski@imse.rwth-aachen.de

¹ Institute for Machine Elements and System Engineering, Schinkelstr. 10, 52062 Aachen, Germany

² Chair of Integrated Digital Systems and Circuit Design, Mies-von-der-Rohe-Str. 15, 52074 Aachen, Germany

lished condition monitoring systems for plain bearings are usually retrofitted to the machine element and need external wiring for data transmission as well as energy supply [4]. To date, there is no condition monitoring system for plain bearings that fully fulfills the characteristics of a SiME.

SiME offer the potential to drive digitalization in mechanical engineering by integrating sensory functions into standardized machine elements [5]. By enabling in-situ monitoring, SiME can significantly enhance the quality of achievable information data by reducing measurement uncertainties as a result of a minimized transfer path [6]. SiME are space-neutral compared to conventional, purely mechanical machine elements to enable simple installation in the target system [7]. Furthermore, SiME are designed to operate autarkic without needing external wiring [8]. To achieve autarky, the sensor data measured is processed by a microcontroller integrated into the machine element, and the data is transmitted wirelessly via an integrated antenna. The electrical energy is supplied by energy harvesting methods, generating electricity from existing environmental conditions. Due to the use of low-cost components, SiME can potentially be widely deployed at critical process points in machines and drivetrain systems. Ideally, they allow immediate online detection and transmission of critical operating points and imminent damage to the respective machine element.

The goal of the research project “Auto-informative Plain Bearings” was therefore to create a Sensor-integrating Plain Bearing (SiPB). The SiPB prototype was developed in the following order of development stages: The initial definition of the requirements led to the development of partial solutions for the sub-functions (condition monitoring, energy harvesting, wireless data transmission) of the SiPB [9]. This was followed by the simulative conceptual design, which is described in detail in [4]. Based on simulative investigations a model-based temperature sensor density was defined to monitor the relevant temperature field and the optimal positioning of TEGs to utilize the maximum temperature differences occurring in the plain bearing. This was followed by the conceptual design of the hardware prototype, which is described in detail in [2]. The selected partial solutions for the sub-functions of the SiPB proved to be promising in the investigations carried out, although a need for further research became apparent.

The pursued CMS approach of temperature field-based lubrication gap height determination via the Gmbel-curve is only valid for stationary conditions. Accordingly, so far only stationary conditions have been considered in the investigations for the selected condition monitoring approach. Additionally, the high spatial resolution of the temperature field monitoring approach may also allow the reliable, on-line detection of mixed friction and incipient damage. This paper provides an overview of the design process of the

CMS with a particular focus on testing the condition monitoring approach particularly for highly transient operating conditions and the special event of lubricant failure.

Besides monitoring highly transient operating conditions the SiPB needs to fulfill the characteristics of energy autarky in each operating condition to be a Sensor-integrating Machine Element. Therefore, the energy harvestable by utilizing the waste heat using a plain bearing integrated thermogenerator will be investigated experimentally. The state of thermal equilibrium is the most disadvantageous state for thermoelectric energy harvesting, as the temperature differences that can be used in the system are minimized. Therefore, the focus for the experimental investigation of the energy harvestable is on stationary operating conditions.

To provide the reader with a comprehensive insight into how the project idea emerged, the following state of the art provides a systematic presentation and classification of the suitability of established methods as partial solutions for the sub-functions of a SiPB. The systematic review of the solutions used for the sub-functions is necessary to understand that the design decisions made are relevant for the following investigations presented in the following paper. In the state of the art the operationally safe design and established condition monitoring methods for hydrodynamic radial plain bearings are stated. Energy harvesting methods are classified regarding their suitability for use in plain bearings and established wireless data transmission protocols for sensor networks are presented.

2 State of the art

2.1 Operation safe design and failure mechanism of hydrodynamic radial plain bearings

DIN-standard 31652 and VDI-standard 2204 establish guidelines for the operation-safe design of hydrodynamic radial plain bearings [10–13]. In the DIN-standard, the Reynolds’ equation [14] is solved for discrete operating points. DIN-standard 31652-2 includes the Gmbel-curve, which provides a relationship between the input parameter shaft misalignment angle β and the output parameter shaft eccentricity ε . In publications associated with the project “Auto-informative Plain Bearings”, it was shown that β in (quasi-)stationary operation highly correlates with the bearing angle of the maximum occurring temperature within the bearing [2, 4]. The lubrication gap height h_{\min} can be determined for an inner bearing diameter d using Eq. 1, if the relative bearing clearance ψ_{eff} is defined:

$$h_{\min} = 0.5 \cdot d \cdot \psi_{\text{eff}} \cdot (1 - \varepsilon) \quad (1)$$

A safe hydrodynamic condition is achieved when the minimum lubrication gap height h_{\min} exceeds a limit value based on surface roughness [15, 16]. Besides the lubrication gap height h_{\min} , the bearing temperature is another critical parameter. As the bearing temperature increases, the mechanical strength and hardness of the bearing material diminishes. Due to their lower melting temperatures, the impact is particularly increased in the case of soft bearing metals (e.g. tin-based babbitt metal). Furthermore, the lubricant viscosity decreases with increasing temperature. Exceeding the temperature limit may also lead to subsequent thickening of lubricant due to chemical reactions, which can cause severe damage to the plain bearing. DIN-standard 31652-3 specifies temperature limits, which represent general empirical values. The relevant measured variable, which is compared with the limit values $T_{B,\text{lim}}$, is the lubricant outlet temperature T_{ex} of the plain bearing [13]. The temperature safety of a tribological system is highly dependent on the solids and lubricant involved. The exact limit of temperature safety must therefore be determined for each specific target system.

However, these standards only address the regime of fluid friction. Operation of plain bearings in the mixed friction range is not covered by the established standards. Nevertheless, plain bearings are increasingly being utilized in applications where operation in the mixed friction zone is unavoidable, such as start-stop processes in the automotive sector [17] and wind turbine operations during run-up, idling, or emergency stops [18]. Run-up processes for example are ensured by adherence to conservatively chosen threshold values for the specific pressure ($\bar{p}_{\text{max}} = 2.5 \text{ MPa}$) of the bearing [13]. Due to the specified limit value, the use of plain bearings in the operation of a wind turbine, for example, would presumably not be feasible according to the established standards.

In the event of adhesion-related bearing damage, the bearing and shaft heat up locally due to progressive mixed friction. Adhesive wear in bearing usually occurs under the condition of lack of lubricant and is associated with a breakdown of the lubricating film between shaft and bearing [19–21]. A welding process of the materials occurs with subsequent separation of the components due to the continuous rotating movement [19]. This cyclical process is repeated until the acting energy is no longer sufficient to overcome the friction at the seizure points or to loosen the welded parts. Adhesion processes cumulatively lead to overheating failure (“seizure”), which is accompanied by a rapid increase in temperature and high flash temperatures in the plain bearing. In the case of abrasive wear, roughness peaks of the harder shaft penetrate into the surface layer of the softer plain bearing and cause micro-cutting as well as material removal [22]. In contrast to overheating failure, abrasive wear progresses slowly and causes a less

rapid, more homogeneous temperature increase in the bearing volume.

The implementation of condition monitoring methods can ensure the identification and control of these non-standardized operating conditions. By identifying potentially critical operating conditions, countermeasures can be implemented to prevent fatal damage to hydrodynamic plain bearings. For condition monitoring of hydrodynamic plain bearings, measurements based on various physical principles are established [23].

2.2 Condition monitoring methods for plain bearings

Established measurement principles for plain bearings include lubricant, friction torque, acoustic emission (AE), contact resistance monitoring, orbital analysis, acceleration analysis and temperature monitoring. The suitability of the established monitoring methods for sensor integration is displayed in Fig. 1.

The measurement principles of lubricant monitoring, friction torque measurement and AE are performed ex-situ. Contact resistance monitoring depends on a constructive adaptation of the target system through electrical insulation of the components. Orbital analysis using inductive or capacitive distance sensors is associated with very high costs (inductive sensors: approx. 10,000€ per monitored bearing). In addition, the displacement sensors are sensitive to adverse environmental influences and must be installed in the lubrication gap to detect changes in the shaft position. Acceleration measurements can only detect late-stage damage and cavitation in plain bearings. A detailed explanation of the condition monitoring principles and the classification with regard to their suitability for SiME application can be found in [7].

In the context of developing a Sensor-integrating Plain Bearing temperature monitoring is an established measuring principle, which excellently fulfills the requirements of the SiME application. Small, ultra-low energy-demand temperature sensors are available on the market, which can be fully integrated into the volume of the plain bearing. Regarding the SiME application, bearing-integrated temperature sensors offer further advantages such as low unit costs, robustness against environmental influences and simple data processing. In the industry standard, usually only the lubricant outlet temperature T_{ex} of the bearing is measured. To ensure the highest sensitivity level of the temperature sensors, the distance between the sensor and the point of friction (load zone of the bearing running surface) must be minimized. Bearing-integrated temperature sensors offer the advantage over the established lubricant outlet temperature measurement that the transfer path is significantly reduced. Therefore, the sensitivity of the bearing-integrat-

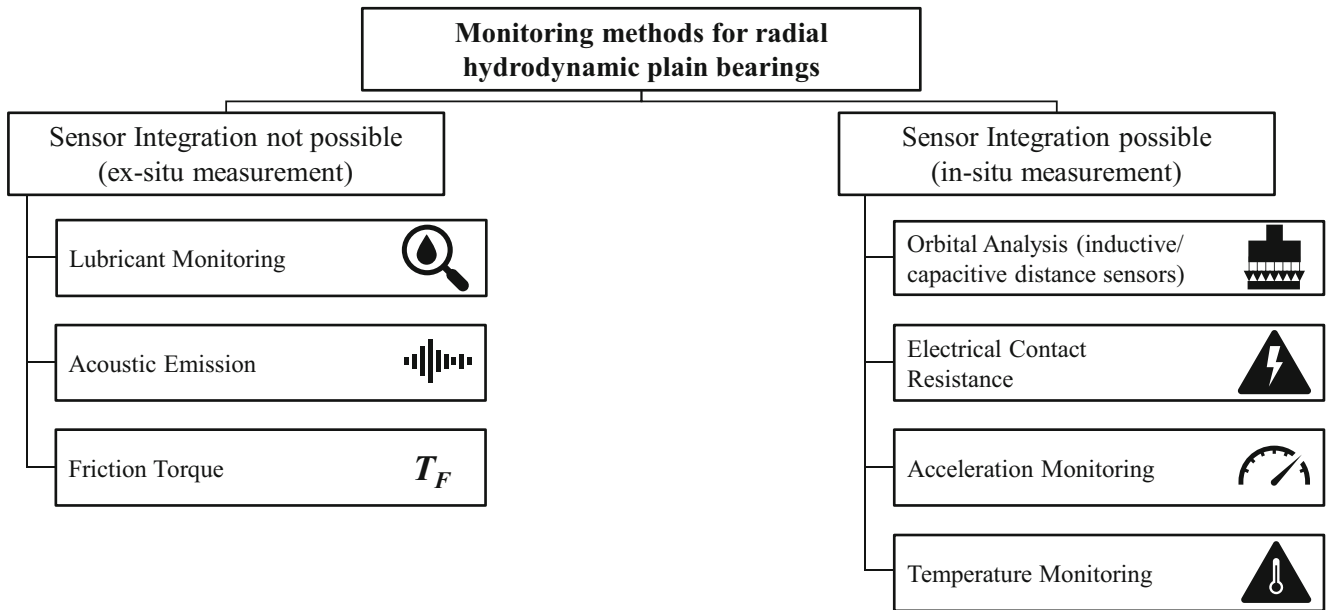


Fig. 1 Suitability for sensor integration of established condition monitoring methods for hydrodynamic plain bearings [7]

ing temperature sensors to occurring wear and emerging damage is highly increased.

A novel CMS approach for creating a SiPB is adapting the established temperature monitoring by measuring the temperature field within the plain bearing. Like the conventional temperature measurement, the novel temperature field measurement approach offers SiME-specific advantages such as low energy consumption and simple data evaluation. High-resolution spatial temperature measurements can minimize the distance to the location of friction occurring within the bearing. Therefore, the temperature field monitoring has the potential to reliably measure mixed friction in real time.

2.3 Energy Harvesting methods

SiME require electrical power supply to record, process and transmit data. According to the definition of the term SiME, no external wiring is permitted. Batteries can be integrated into the SiME, however they are discharged over time. Therefore, in the SiME context, the use of energy harvesting (EH)-methods is a viable option for achieving permanent energy autarky. Energy harvesting devices generate electrical energy to power low-energy microelectronics by utilizing ambient energy from occurring energy sources [24]. In Fig. 2 established EH-methods, which could be suitable for SiME-applications are displayed.

However, most of the established EH-methods are not suitable for harvesting electrical energy within a plain bearing. In plain bearing the usual occurring mechanical loads are too static for piezoelectric EH. Therefore, piezoelectric EH is more suitable for dynamically loaded machine

elements, like gears or roller bearings. For the SiPB application photoelectric EH is not a viable option as plain bearings are usually located inside a housing without internal light sources. Triboelectric harvesting of sufficient amounts of energy to power microelectronics is only possible in intense mixed friction, which represents a potentially damage-critical state of the plain bearing. For the SiPB application, triboelectric EH would therefore only be suitable as support for another EH method to provide additional electrical energy for the power-intensive wireless transmission of an alarm signal in the event of a critical operating state. In general, the electromagnetic EH approach is suitable for utilizing the mechanical energy generated by the relative movement of the plain bearing and shaft to generate electrical energy. However, a driving magnet must be incorporated into the shaft for the electromagnetic energy harvesting approach. This contradicts the characteristics of a SiME, as the target system is changed by the insertion of the magnet into the shaft. Therefore, electromagnetic energy harvesting cannot be used for the design of a SiPB.

The final EH method to be presented is thermoelectric EH. Thermoelectric EH is ideal for SiPB applications. In the plain bearing, heat is generated by the relative movement of the shaft and the resulting friction. This waste heat occurring can be converted into electrical energy using microelectronic devices called thermoelectric generators (TEG), which work based on the thermoelectric EH principle. Thermoelectric energy can even use small temperature differences in the range of a few Kelvin to generate electrical energy [32, 33]. TEGs are low-cost, off-the-shelf microelectronic components consisting of semiconductors to harvest electrical energy from heat sources [34,

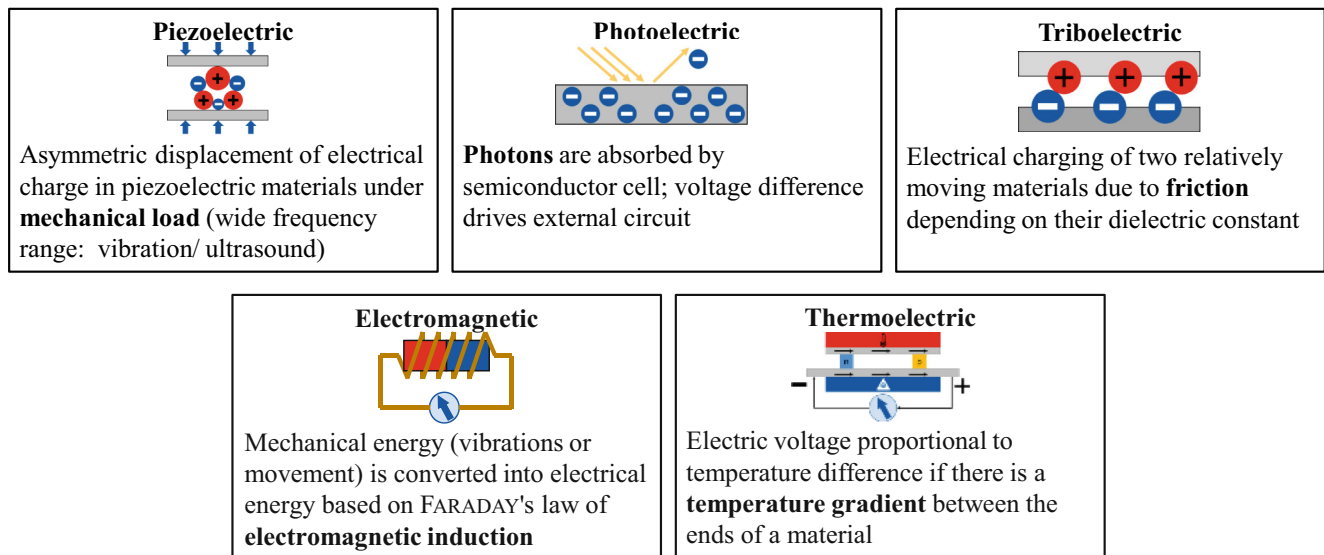


Fig. 2 Established energy harvesting methods [25–31]

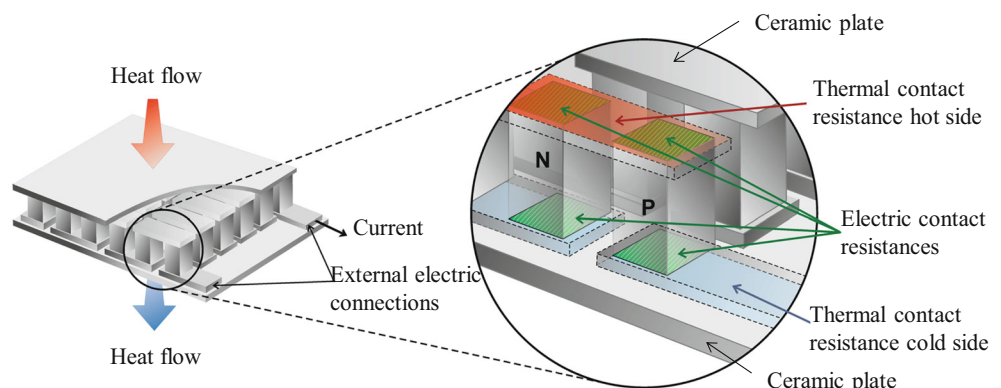
35]. TEGs are usually designed in a cuboid shape. Figure 3 schematically displays the design of a TEG, which is made up of thermoelectric pairs of *n*- and *p*-type semiconductors.

If there is a temperature difference between the ceramic plates and heat flows through the TEG resultingly, a voltage is present at the external electrical connections which can be used to generate electrical energy. For the application of thermoelectric EH in plain bearings, one challenge is the relatively low temperature gradients occurring within the plain bearing volume. The output voltages of TEG are in the range of 50 mV per K, depending on the number of series-connected semiconductor within the TEG [37]. Resultingly, in the range of low level-heat with small thermal gradients occurring the output voltage of TEG is usually beneath the minimum input voltage to supply a wireless communication module [38, 39]. Energy harvesting methods are often used for sensor networks that operate with operating voltages of 1.8 to 3.3 V [40]. Since microelectronics require a constant and stable voltage for their operation, the fluctuating output voltage of the EH modules, which is directly dependent on

the temperature differences present, poses a challenge. To ensure a constant supply to the sensors, DC/DC converters are therefore needed to convert the varying input voltage of the TEG into a defined output voltage.

The commercial market offers DC/DC-converters that support an input voltage of a few 10 mV up to a maximum of 300–500 mV. A minimum input voltage of 20 mV is needed for the self-start of these converters. The output power is in the range of a few 100 μA. State-of-the-art DC/DC-converters also offer the possibility of using several independent energy sources. For example, one circuit can be used for the operation of sensors and data management, while another circuit is used for charging a battery as an energy buffer for storing surplus energy. Surplus energy is generated at times when the energy production exceeds the consumption of the entire system. At times of increased energy consumption (e.g. power-intensive alarm transmission), energy buffers can compensate for the deficit. Possible energy buffers for autarkic systems are rechargeable batteries and supercapacitors [37]. In terms of energy stor-

Fig. 3 Schematic structure of a Thermoelectric Generator [36]



age integration to the SiPB, the temperatures that occur during operation must be considered. Batteries designed for high-temperature applications are part of current scientific research. In their review paper, Kumaravel et al. report on current research that defines hydrogels and ionogels as suitable solid electrolytes for high-temperature batteries and supercapacitors. Temperatures of up to 200 °C are indicated as possible levels of application [41].

2.4 Wireless data transmission

To achieve complete autarky of a SiME, measurement data processing using a machine element-integrating microcontroller and wireless transmission of data and alarm signals are required. In the future SiME should act as a part of a wireless sensor network (WSN) in industrial applications. For WSN a variety of transmission standards that can be scaled according to the application scenario and energy requirements are established [42]. For communication over long distances the 5G mobile communications standard provides for energy-efficient transmission for sensor devices. There are also several other industry standards, such as narrow-band IoT. A key aspect of WSN is energy efficiency, which is achieved by implementing relatively lean protocols resulting in smaller data packets. However, relatively high instantaneous power remains during transmission [43]. Shorter distances with lower power consumption are offered by the WLAN or Bluetooth standard. The latter is now widely used in the field of sensor networks. One prominent example is the so-called Bluetooth (BT) beacon. Such BT beacons can achieve battery lifetimes of over 10 years. Well-known everyday examples of BT beacons are tracking devices such as the Apple Airtag. In this case, the unidirectional communication channel needs to be considered, which can save a significant amount of energy thanks to very short active phases. The wireless interface of a SiME must ultimately support three application scenarios: transmission of sensor data, transmission monitoring alarm and update capability of the software. The software's update capability enables the adjustment alarm limit values or the CMS sampling rate continuously during operation.

2.5 Interim conclusion

Hydrodynamic plain bearings are increasingly being used in operating conditions that are not covered by established design standards. With information provided by a CMS condition-based maintenance actions can be implemented to prevent damage at an early stage and reduce machine downtime. In the context of SiME, temperature-based condition monitoring is an excellent established method for plain bearing monitoring. To further increase the sensitivity of detecting mixed friction, the temperature field of the

plain bearing can be monitored. Of the established energy harvesting methods the only suitable method for permanent plain bearing-integrated energy harvesting is thermoelectric energy harvesting. The integration of a microcontroller with an integrated data antenna is necessary for data processing and transmission. A large number of data protocols are established in this area. With regard to the microcontroller, a hardware solution should be selected that is as energy efficient as possible and can send data and alarms with the highest possible signal strength. WLAN and Bluetooth Low Energy are particularly energy-efficient protocol solutions for WSN systems.

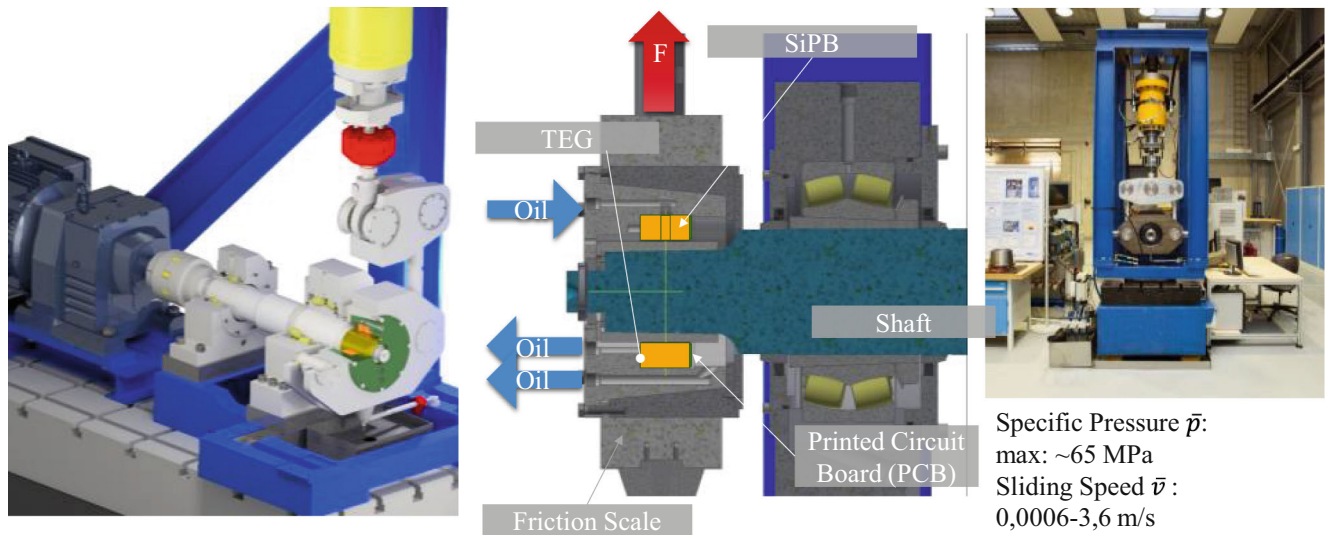
3 Objective and approach

The presented work addresses the capability of the developed SiPB-prototype regarding monitoring transient operating states and whether thermoelectric EH is able to provide sufficient energy to power the SiPB in stationary operating states. Sect. 4 describes the test setup used for the experimental and simulative investigations in the following chapters. The principle of temperature field-based gap height determination to monitor abrasive wear in quasi-stationary operation conditions of plain bearings has been investigated in [2, 4]. Therefore, the focus of Sect. 5 will be on the suitability of the temperature field-based approach for monitoring transient operating conditions and the special case of lubricant supply failure, which are both potentially causing rapid adhesive failure. By establishing appropriate limit values, it will be demonstrated that temperature field measurements can effectively monitor all relevant operating conditions present in the plain bearing.

Only thermoelectric EH is suitable for permanently harvesting electrical energy to operate the SiBP using EH methods as well as fulfilling the characteristics of a SiME. Sect. 6 presents experimental results of the thermoelectrically harvestable energy in plain bearing operation. Here, stationary operation is considered in which a thermal equilibrium develops in the test bench system. As a result, a very small temperature gradient is formed on the plain bearing-integrated TEG, which represents the most critical state for thermoelectric energy harvesting regarding the energy harvestable. Finally, the results depicted are summarized and an outlook on future investigations is given.

4 Test setup

The experimental investigations of temperature field-based condition monitoring and thermoelectric harvestable energy are conducted on a test rig for hydrodynamic plain bearings, which is described in detail in [9]. A bronze alloy



Specific Pressure \bar{p} :
 max: ~65 MPa
 Sliding Speed \bar{v} :
 0,0006-3,6 m/s

Fig. 4 Schematic illustration of the test rig assembly

plain bearing manufactured from CuSn12Ni2 (85% copper and 12% tin) was used for the tests. The plain bearing has an inner diameter of $d=120\text{ mm}$ and a width of $b=30\text{ mm}$. The lubricant used was a synthetic gear oil of ISO VG class 320. The shaft sleeve, which is in tribological contact with the test plain bearing, is made of hardened steel (material: 42CrMo). The bearing clearance is $e=140\text{ }\mu\text{m}$ (relative bearing clearance $\psi=1.1667\text{ ‰}$). Figure 4 schematically illustrates the test setup used.

During operation, the plain bearing is positioned within a friction scale via which the radial test force is applied by a hydraulic cylinder. The friction scale is mounted freely so that the friction torque occurring in the test plain bearing is measured during the test via a connected load cell. The shaft is supported by two roller bearings and driven by a 250-kW electric motor. The lubricant supply for the hydrodynamic lubricating film build-up of the plain bearing is provided via

a lubrication groove at the top of the plain bearing (bearing angle $\varphi=0^\circ$).

The prototype was developed to fulfill the requirements of a SiME. For this purpose, only market-available micro-electronic components were considered and integrated into the plain bearing volume. Figure 5 shows the SiPB-prototype and the integrated electronic components.

To achieve future autarky of the SiPB to be developed, a microcontroller for data processing integrated into the machine element and a WLAN interface for wireless data transmission were implemented. When investigating the wireless transmission of operating data from the SiPB during test bench operation, it was observable that the signal could be transmitted at full strength from the metallic housing using various hardware solutions. Existing joints and non-metallic components enable the signals to be transmitted out of the housing. Ultimately, a hardware and software

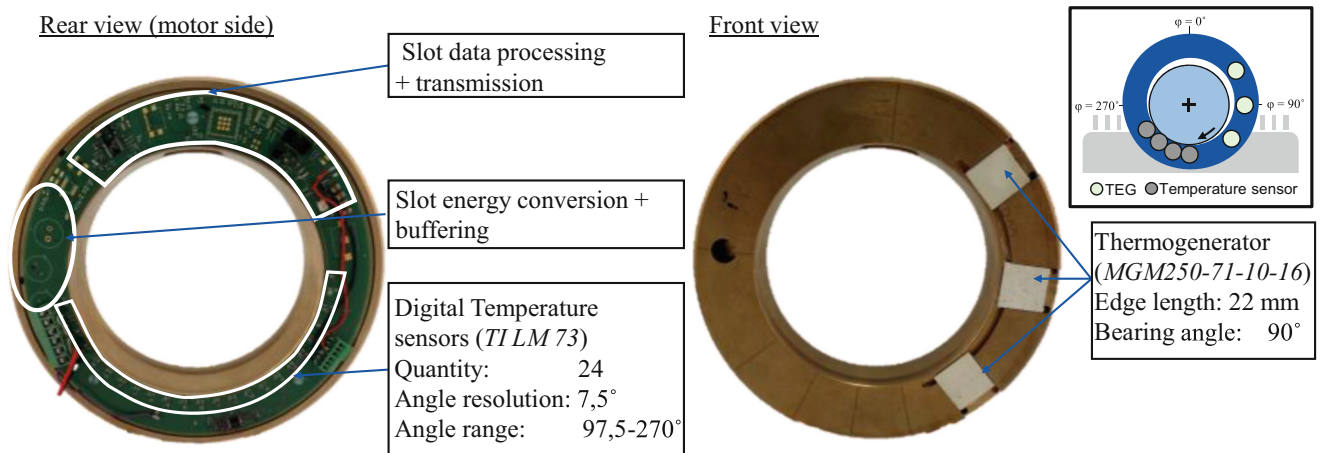


Fig. 5 SiPB-Prototype

solution must therefore be selected that enables stable data transmission with minimal energy consumption. As data transmission is an engineering challenge, the “Data Transmission” sub-module is not addressed separately in this paper.

Furthermore, TEGs, which generate electrical energy from waste heat were integrated into the plain bearing (see Fig. 5 right). The simulative determination of the optimum TEG positioning is documented in [4]. DC-DC converters are connected to the printed circuit board (PCB) to provide the necessary operating voltage for the microelectronics and supercapacitors for energy buffering. For condition monitoring, 24 digital temperature sensors are integrated on the PCB along the circumference of the bearing in the range $\varphi = 97.5\text{--}270^\circ$, which includes the load zone during operation. The temperature sensors are in physical contact with the bearing face due to the screw connection between the PCB and the bearing. The digital temperature sensor TI LM73 used offers a maximum measurement frequency of $f_M = 8.92\text{ Hz}$ at a maximum possible temperature resolution of $\Delta T_{\text{res}} = 0.03125^\circ\text{C}$ [44]. The PCB is completely integrated into the construction volume of the plain bearing. To improve heat transfer and therefore the response behavior of the temperature sensors, thermal paste is applied between the sensors and the bearing. The minimum distance from the measuring point to the running surface is 1.5 mm. The sensitivity of the temperature measurement could be further raised by applying thin-film sensors directly onto the running track. However, thin-film sensors are costly custom-made products. Also, thin-film sensors bear the risk that they could be damaged by mixed friction

occurring. Therefore, the chosen approach is much more robust than thin-film sensors from a financial point of view and especially when measuring mixed friction conditions. The exact microelectronic components used in the SiPB-prototype are documented in [2].

5 Temperature field-based Condition Monitoring

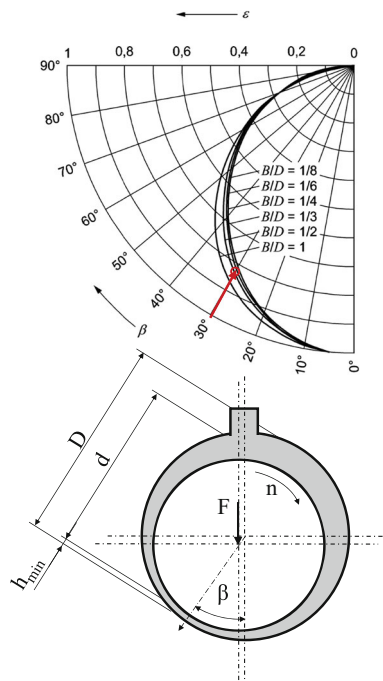
In this chapter the temperature field-based, in-situ approach to monitor hydrodynamic plain bearings is examined. First, the implementation of the Gumbel-curve to the bearing-integrated controller to monitor the lubrication gap height is briefly described in Sect. 5.1. Section 5.2 presents experimental results of the CMS for transient operating conditions in the form of start-stop tests. Sect. 5.3 examines the possibility of detecting the special event of a lubricant failure based on simulative investigations.

5.1 Gap height determination via Gumbel-curve

The Gumbel-curve is displayed in tabular and graphical form within the DIN standard 31652 to determine the eccentricity of the shaft ϵ . Figure 6 illustrates the Gumbel-curve for the bearing geometry investigated in graphical form on the left-hand side and in tabular form on the right-hand side.

Measuring the bearing angle of the maximum temperature occurring in vicinity of the running surface enables the detection of the displacement angle β . The pairs of values

Fig. 6 Concept of the Gumbel-curve for hydrodynamic radial plain bearings [11]



| | | | | |
|------------------|-------|-------|-------|-------|
| $\beta [^\circ]$ | 0 | 2.85 | 5.73 | 7.7 |
| $\epsilon [-]$ | 1 | 0.999 | 0.995 | 0.99 |
| $\beta [^\circ]$ | 10.38 | 12.4 | 14.11 | 15.63 |
| $\epsilon [-]$ | 0.98 | 0.97 | 0.96 | 0.95 |
| $\beta [^\circ]$ | 21.79 | 31.25 | 39.33 | 46.83 |
| $\epsilon [-]$ | 0.9 | 0.8 | 0.7 | 0.6 |
| $\beta [^\circ]$ | 54.07 | 61.21 | 68.3 | 75.39 |
| $\epsilon [-]$ | 0.5 | 0.4 | 0.3 | 0.2 |

Bearing data: $B/D = 0.25$;
 Bearing diameter $D = 120\text{ mm}$;
 Bearing width $B = 30\text{ mm}$;
 Bearing Clearance $e = 140\text{ }\mu\text{m}$; Relative bearing clearance $\psi = 1,1667\text{ ‰}$

shown in the table in Fig. 6 can be approximated using Eq. 2 with a coefficient of determination $R^2=1$.

$$\begin{aligned} \varepsilon_{G\u00fcmbel} = & -1 * 10^{-8} * \beta^4 \\ & + 3 * 10^{-6} * \beta^3 \\ & - 0.0003 * \beta^2 \\ & + 0.0012 * \beta + 0.999 \end{aligned} \tag{2}$$

Equations 1 and 2 can be implemented on the plain bearing-integrated microcontroller for continuous, computationally efficient temperature field-based lubrication gap height calculation. Under steady-state operating conditions, the temperature field-based lubrication gap height can be continuously compared with the roughness-based limit values according to ([11]; Eq. 3) or ([16]; Eq. 4), which indicate the transition from the liquid friction area to the mixed friction area.

$$h_{min} = (0.5 \dots 1.0) * \sqrt{Rz_{Shaft}^2 + Rz_{Bearing}^2} \tag{3}$$

$$h_{min} = 3 * \sqrt{Rq_{Shaft}^2 + Rq_{Bearing}^2} \tag{4}$$

The limit values are determined by the roughness values in the initial state of the bearing. The values can continuously be updated on the microcontroller to account for running-in processes and associated roughness smoothing of the bearing. In addition, mixed friction causes a local temperature increase, which can also be determined by the selected CMS-approach.

5.2 Transient operating conditions

The concept of temperature field-based lubrication gap height determination via the G\u00fcmbel-curve is only valid for quasi-stationary operating conditions. In preliminary investigations, which are presented in this chapter, it will be proven that the CMS sensor setup can also monitor highly transient conditions, such as start-stop conditions, well. The temperature sensor setup is sensitive enough to detect changing friction conditions quickly. The sensor concept is thus also capable of dynamically detecting rapid temperature changes, which occur in the event of spontaneous adhesive failure of plain bearings.

To investigate the sensitivity of the sensor concept to transient conditions, a start-stop test, which replicates the load conditions of a planetary plain bearing in wind turbines, was conducted on the test rig shown in Fig. 4. The start-stop test consists of 40 cycles of 99s each ($t_{total}=3960s=1.1h$). Within the first 30s of the cycle, the sliding speed is increased linearly to $\bar{v}=2.5m/s$ from standstill. In the range $t_{cycle}=[15s, 30s]$, the specific pressure \bar{p} is increased from 0.1388 to 10MPa. The maximum values of \bar{v} and \bar{p} are maintained until $t_{cycle}=60s$. Then \bar{v} is reduced linearly in the range $t_{cycle}=[60, 90s]$ until standstill. The maximum pressure $\bar{p}=10MPa$ is maintained till $t_{cycle}=93s$ and reduced linearly to $\bar{p}=0.1388MPa$ until $t_{cycle}=99s$ (see Fig. 7). This procedure is repeated until the final 40th cycle is reached, and the test is then terminated as scheduled.

Figure 8 (upper half) illustrates the temperature signals recorded by the SiPB-prototype over time as well as the oil outlet temperature T_{ex} . The oil supply temperature for the experiment shown in Fig. 8 is $T_{in}=20^\circ C$. A sampling rate of $f_M=0.14Hz$ was used in the test.

The individual cycles of the start-stop test are clearly identifiable in the recorded temperature signals of the SiPB-prototype. Each start-up process is accompanied by a rel-

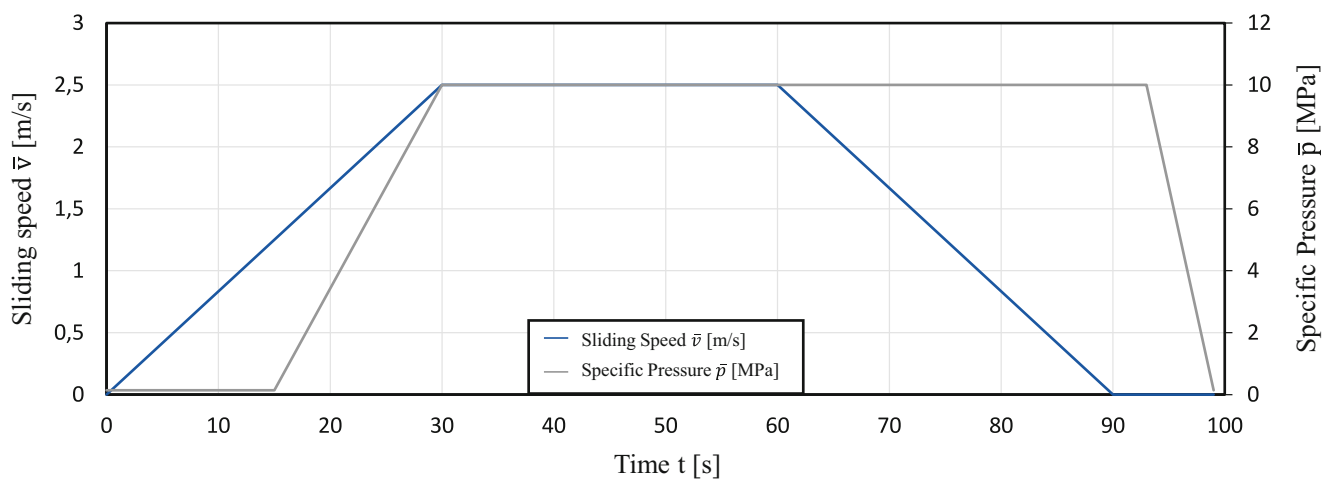


Fig. 7 Operating conditions start-stop test (40 cycles á 99s)

actively steep temperature increase for all 24 measuring points in the plain bearing. When the maximum specific pressure ($\bar{p}_{max} = 10\text{MPa}$) and maximum sliding speed ($\bar{v}_{max} = 2.5\text{m/s}$) of each cycle are reached, a local temperature maximum is obtained at all temperature measuring points over time. The reduction of the sliding speed \bar{v} and subsequent reduction of the specific pressure \bar{p} at the end of each cycle is accompanied by a negative temperature gradient in the time domain at all measuring points. The end of the stop process of each cycle is accompanied by a local minimum of the respective temperature measurement signals. At the start of the following cycle, the described temperature behavior is repeated at all 24 measuring points. In all cycles, the temperature increase in the start process is greater than the following temperature decrease due to the stop process. Accordingly, the increase in thermal energy introduced into the bearing adds up over the entire course of the 40 start-stop cycles, causing the average temperature curve to approach a maximum level asymptotically.

Compared to the recorded oil outlet temperature T_{ex} in Fig. 8, which is used to assess the temperature safety of plain bearings in accordance with DIN 31652 (see Sect. 2.1), it is observable that the temperature field monitoring approach is significantly more sensitive to the detection of transient operating states and the associated changing friction caused by the start-stop-processes. From the course of T_{ex} it is evident that the first start-stop cycle has almost no effect on T_{ex} . Only at the beginning of the second cycle after around $t = 100\text{s}$ testing time an increase in

T_{ex} is recognizable. T_{ex} subsequently follows a degressively increasing curve. In contrast to the measurements of the temperature field in the plain bearing, the individual cycles are not visible in the T_{ex} -curve. Figure 8 (lower half) shows the friction torque T_F within the plain bearing recorded over the course of the start-stop test. At the beginning of each cycle, T_F increases rapidly with the start process and reaches its local maximum value. At the beginning of the stop process, the frictional torque decreases again until it reaches its minimum value ($T_F = 0\text{Nm}$) at the end of each cycle when the test rig comes to a standstill. The level of the maximum friction torque reached is relatively constant for all 40 cycles ($T_{F,max} \approx 38\text{Nm}$). After reaching the $T_{F,max}$ -value during the starting process, no further increase in friction torque T_F caused by the subsequent stopping process can be observed at the end of all cycles. Therefore it can be assumed that increase in friction torque was due to fluid friction, which was predominant during the whole test cycle. This is due to the relatively low specific pressure ($\bar{p}_{max} = 10\text{MPa}$), high sliding speed ($\bar{v}_{max} = 2.5\text{m/s}$) as well as smoothed bearing running surface due to prior tests with the SiPB-prototype.

In order to enable precise differentiation of damage-inducing and damage-uncritical operating states using the SiPB, it is necessary to determine robust and reproducible alarm limit values based on the temperature field measurement. On the one hand, the selection of suitable limit values enables imminent damage to be detected in time and countermeasures to be initiated. On the other hand, robust alarm

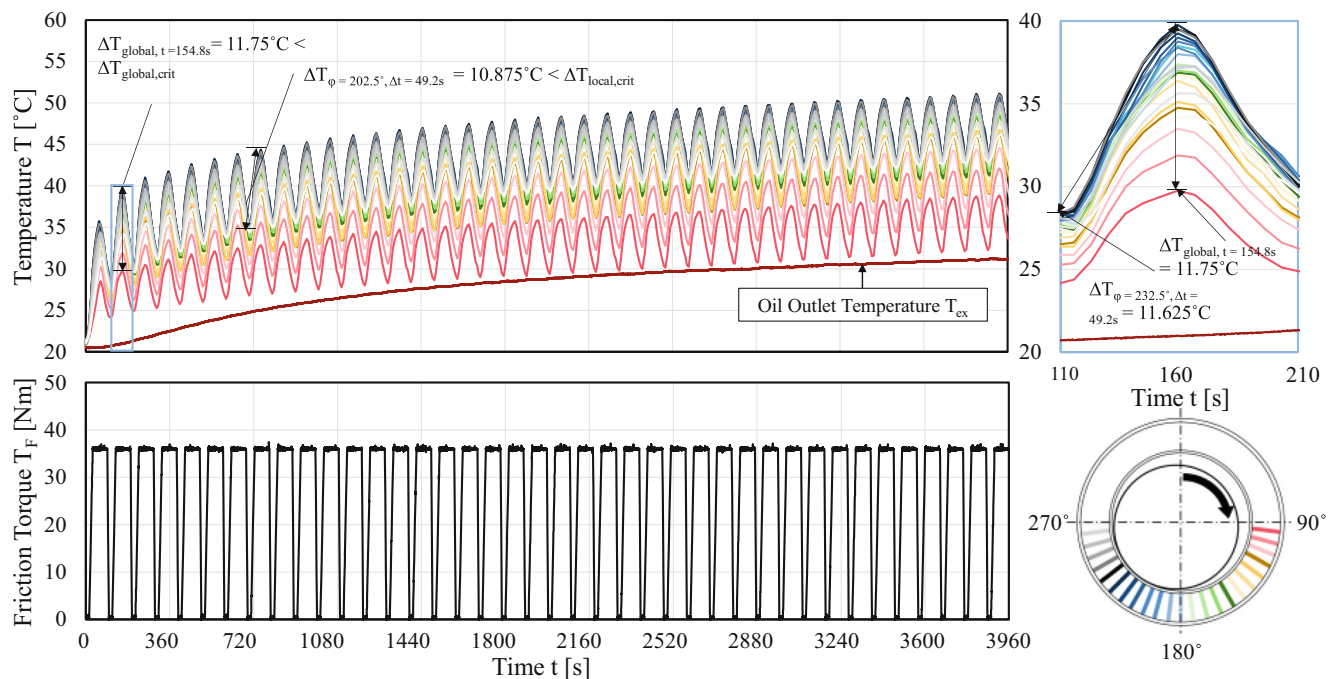


Fig. 8 Start-stop test: temperature curves for each measuring position ($\varphi = 97.5\text{--}270^\circ$) and oil outlet temperature (upper half) and measured friction torque (lower half), (40 cycles \dot{a} 99 s; $T_{in} = 20^\circ\text{C}$)

limits ensure the avoidance of incorrect damage reports and the associated increased downtimes. Possible features that can be extracted as alarm limit values from the temperature field measurement data are displayed in Fig. 8. In addition to the highest measured temperature $T_{\max, \text{global}}$ at a given time, temperature gradient-based limit values can also be used as alarm limit values, which can be correlated with the thermal heat input into the bearing. The global temperature gradient $\Delta T_{\text{global}, t}$, i.e. the difference between the maximum and minimum measured temperature in the temperature field at a defined point in time, can be used as an alarm limit. Local temperature gradients $\Delta T_{\varphi, \Delta t}$ are also potentially suitable alarm limits. In this case, the temperature increase at a fixed measuring point φ during a defined time period Δt is monitored. These alarm limit values can be determined by experimentally causing severe mixed friction as well as fatal damage to the plain bearing while recording the temperature field and then extracting the characteristic values from the recorded temperature data. Once determined, the alarm values can be implemented in the operating logic of the plain bearing-integrated microcontroller and an alarm signal can be transmitted wirelessly immediately if a limit value is exceeded.

Figure 9 shows a section of the temperature curves shown in Fig. 8 for the second start-stop cycle of the 40 total cycles. The black vertical lines represent the respective measurement times. At the measuring position with the highest occurring temperature, the temperature rises by $\Delta T_{\varphi=240^\circ, 1} = 2.0^\circ\text{C}$ within the first measuring period of the start cycle shown. In the subsequent measurement period, the temperature rises again by $\Delta T_{\varphi=240^\circ, 2} = 2.75^\circ\text{C}$.

Despite the low measurement frequency of $f_M = 0.14\text{ Hz}$, it can be seen that the start-up processes can be recognized by the recorded temperature increases of the SiPB within a sampling step. The temperature curve also indicates that an even faster detection of the change in contact state is possible with a higher sampling rate. In future, it will be necessary to determine the obtainable maximum measuring frequency. In the event of damage initiation, critical conditions can thus be detected more quickly and countermeasures initiated. At the same time, the maximum realizable measuring frequency is limited by the amount of harvestable energy available.

In the field of application, the lubricant of the plain bearing is often heated before supply in order to reduce the viscosity. An increase in the oil supply temperature T_{in} causes the bearing and surrounding structure to be heated up by the lubricant's additional heat flow under otherwise constant conditions. This could have a negative effect on the temperature field measurement, as this results in a more even temperature distribution within the bearing due to the high thermal conductivity of the bronze material used. Therefore, the start-stop test was conducted with an increased oil supply temperature $T_{\text{in}} = 60^\circ\text{C}$. The temperature curves recorded using the SiPB-prototype are shown in Fig. 10.

In comparison to Fig. 8, it is observable that the temperature differences in the measurement field are, as expected, smaller due to the uniform heating of the bearing by the inflowing oil. For example, at $t = 154.8\text{ s}$, the global temperature gradient is at $\Delta T_{\text{global}, t = 154.8\text{ s}} = 5.25^\circ\text{C}$, while at an oil supply temperature $T_{\text{in}} = 20^\circ\text{C}$, it is at $\Delta T_{\text{global}, t = 154.8\text{ s}} = 11.75^\circ\text{C}$ (Fig. 8). Nevertheless, the start and end of each of the 40 cycles can be clearly detected using the temperature

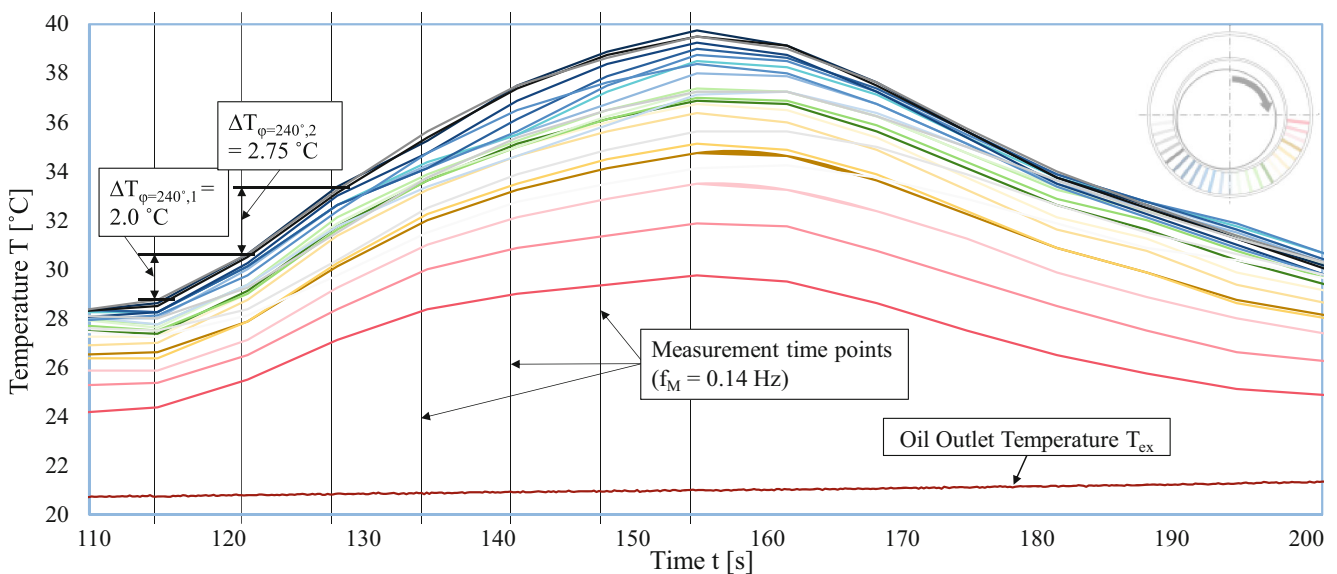


Fig. 9 Start-stop test—2nd cycle: temperature curves for each measuring position ($\varphi = 97.5\text{--}270^\circ$) and oil outlet temperature, (40 cycles á 99 s; $T_{\text{in}} = 20^\circ\text{C}$)

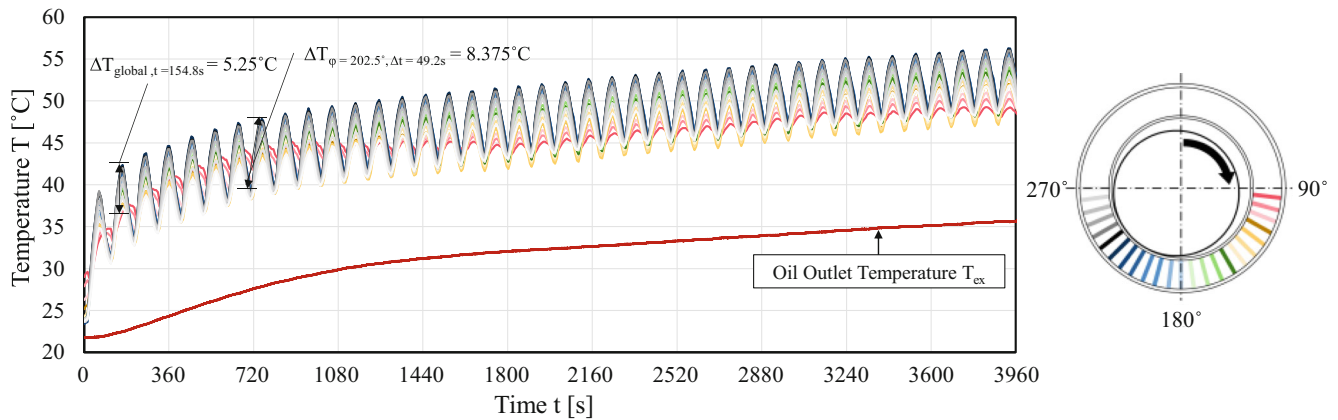


Fig. 10 Start-stop test: temperature curves for each measuring position ($\varphi = 97.5\text{--}270^\circ$), (40 cycles á 99 s; $T_{in} = 60^\circ\text{C}$)

signals. In direct comparison with the recorded temperature level of the temperature field measuring points compared to the oil outlet temperature T_{ex} , the deviation in the temperatures is even greater at a higher oil supply temperature. At the end of the last cycle, the temperature difference between the lowest measured temperature $T_{min,t=3960s} = 48.75^\circ\text{C}$ in the temperature field and $T_{ex,t=3960s} = 36.32^\circ\text{C}$ for the test is displayed in Fig. 10.

A reduction in cycle time might also have a negative impact on the sensitivity of the CMS approach. An additional experiment was therefore conducted where the cycle time was reduced to $t_{cycle} = 35$ s. The measurement frequency was kept constant at $f_M = 0.14$ Hz during the test. The values \bar{v}_{max} and \bar{p}_{max} were kept identical to the two previously presented tests. The oil supply temperature is $T_{in} = 60^\circ\text{C}$. Figure 11 displays the temperature curves for the test with reduced cycle time.

Figure 11 shows that despite a reduction of the cycle time to 35 s, the individual start-stop cycles can be clearly extracted by measuring the temperature field. Due to the shorter cycle time, the thermal energy introduced in a cycle

is lower than in the two previous experiments displayed in Fig. 8 and 10. The local temperature gradients during a cycle are correspondingly lower. Even in the experiment with a shorter cycle time, the temperature level of the temperature field is always clearly above the oil outlet temperature T_{ex} .

In summary, the temperature field measurement approach is very suitable for monitoring highly transient operating conditions of plain bearings. Despite the very low sampling rate of $f_M = 0.14$ Hz, the individual start-stop processes can be clearly recognized from the temperature field measurement data. Depending on the available energy budget, the measurement frequency can be increased. To enable monitoring of the plain bearing and differentiation of critical from non-critical operating conditions, it is necessary to determine alarm limit values based on the temperature field. Due to the high sensitivity of the temperature sensors to changing friction conditions, temperature gradients and total temperature values can be used for this purpose, which can be determined experimentally. For this purpose, a damage criterion, for instance friction torque

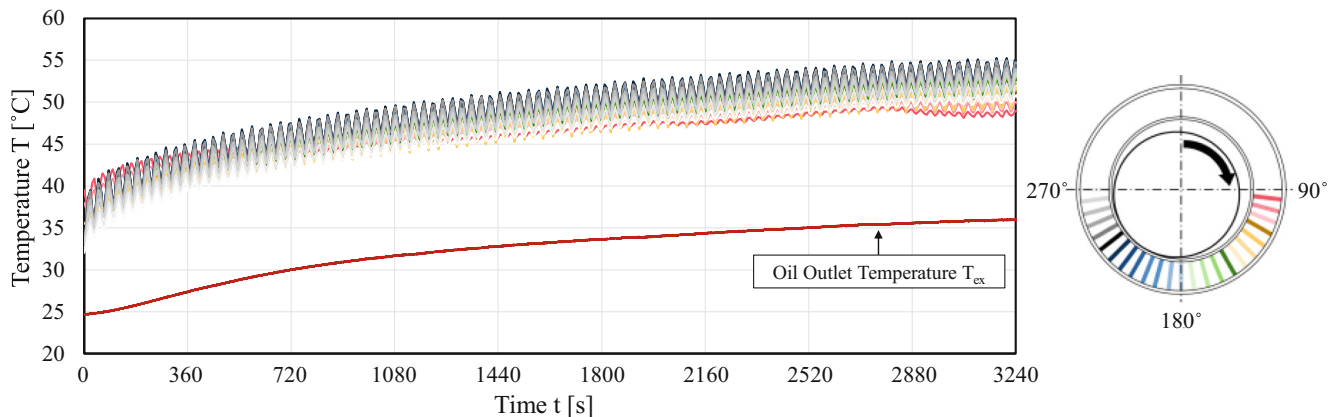


Fig. 11 Start-stop test: temperature curves for each measuring position ($\varphi = 97.5\text{--}270^\circ$), (100 cycles á 35 s; $T_{in} = 60^\circ\text{C}$)

limits, must be defined as the end of the test. The damage can then be induced by measuring the temperature field and alarm limit values can be extracted. It is important to ensure that a sufficiently high number of damage events are carried out so that robust and reproducible alarm limit values can be determined.

5.3 Special incident lubricant supply failure

A special incident that can fatally damage a hydrodynamic plain bearing is the failure of the lubricant supply. In this subchapter, the sensor setup of the SiPB-prototype is simulatively evaluated regarding the ability of early detection of lubricant supply failures in hydrodynamic plain bearings. In the event of lubricant supply failure, the emergency running behavior of the plain bearing determines whether there is an overheating failure of the plain bearing due to adhesion or the plain bearing can continue to operate for an indefinite period without damage (“passer”). The emergency running behavior under constant heat dissipation of the system is mainly dependent on the friction power released in the plain bearing [45, 46].

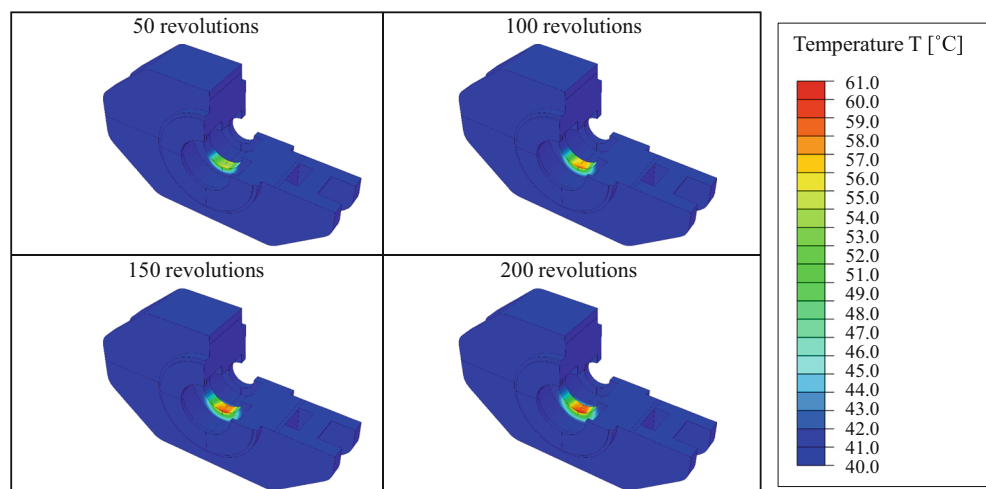
In the event of bearing failure, a rapid increase in temperature is caused in the bearing and bearing temperatures are reached far above the temperature safety limits specified in DIN 31652. In the event of a passer, there is a short-term increase in temperature and the bearing reaches its regular operating temperature after a few minutes. In the case of a passer, an elastohydrodynamic deformation cavity is formed by the remaining oil in the lubrication gap after the lubricant supply is interrupted. Within the cavity created by the hydrodynamic pressure in the load zone enough oil is retained. Even without further lubricant supply, the remaining oil prevents bearing failure despite the occurrence of mixed friction for an undefined time [45].

The simulations that will be presented in this subchapter focus on operating conditions in which a passer is to be

anticipated. The aim here is to test whether the temperature field-based CMS can detect a lubricant supply failure without immediate bearing failure. For simulative investigations, the heat input into the plain bearing caused by frictional power in the case of a passer was determined using a coupled multi-body simulation (MBS) and thermoelasto-hydrodynamic (TEHD) simulation in AVL Excite. The determined heat flows were iteratively imprinted to a thermal FE model in Abaqus to obtain the transient temperature distribution in the plain bearing volume. The simulation models used to depict the test setup presented in Sect. 4 correspond to the models presented in [4]. The simulation conditions were selected in analogy to [45]. At the beginning of the TEHD-MBS, the lubrication gap of the plain bearing is assumed to be fully filled (ISO VG320 gearbox-oil). The oil supply flow is set to a constant volume flow of 0l/min, so that the kinematics of the system cause oil to exit of the lubrication gap successively and no new oil is supplied. In analogy to Marheineke [45], 200 shaft revolutions were simulated. The heat flow calculated in AVL Excite is applied to the plain bearing was imprinted on the running surface of the FE model after each shaft revolution. The FE simulation for calculating the temperature distribution in the plain bearing volume is carried out in 200 steps, in which the new temperature distribution is determined after each shaft revolution and the consecutive heat flow from the TEHD-MBS is subsequently applied.

An oil and initial bearing temperature of $T_{in} = T_{bearing} = 40^{\circ}\text{C}$ was selected for the TEHD-MBS. The specific pressure $\bar{p} = 5\text{MPa}$ and the sliding speed $\bar{v} = 3.5\text{m/s}$ were kept constant over the simulation duration. The operating conditions selected are in the purely hydrodynamic range according to DIN 31652. Figure 12 displays the temperature distribution within the plain bearing and surrounding friction scale within the FE simulation after 50, 100, 150 and 200 revolutions. 200 revolutions correspond to a duration of $t = 21.5\text{s}$ at the sliding speed \bar{v} investigated.

Fig. 12 Temperature distribution of the plain bearing and friction scale after 50, 100, 150 and 200 shaft revolutions



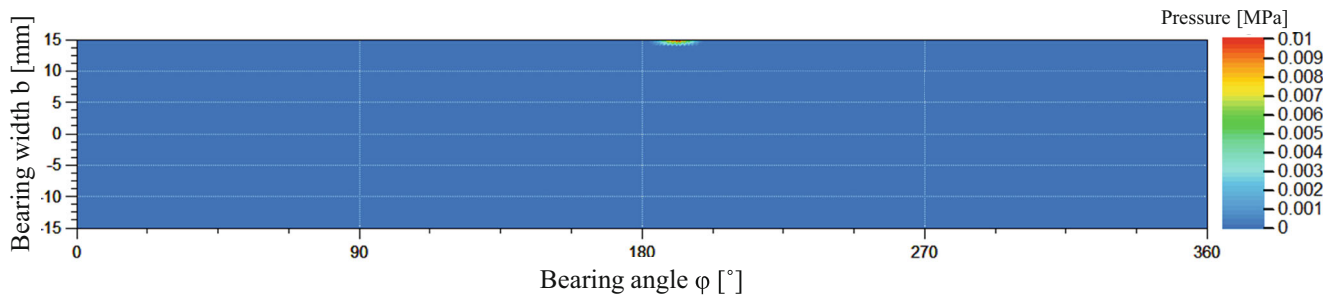


Fig. 13 Solid body contact pressure distribution after 200 shaft revolutions after lubricant supply failure

It is evident that in the load zone (angular position around $\varphi = 180^\circ$) there is a local temperature increase within the bearing volume. As the radial distance of the shaft from the running surface increases, the temperature in the plain bearing gradually decreases. The maximum temperature occurring on the running surface after 200 revolutions is $T_{\max} = 60.37^\circ\text{C}$, so that a passer without bearing failure can be assumed. Figure 13 shows the associated solid contact pressure distribution after 200 revolutions in the case of failure of the lubricant supply.

The solid contact pressure is only very low compared to the total pressure of approx. 25 MPa in the load zone. The course of the maximum bearing temperature over the simulated time with a failure of the lubricant supply is displayed in Fig. 14 top by the orange solid line. In addition, the temperature curve of a simulation with a constant oil supply ($p_{\text{supply}} = 0.2\text{ MPa} = \text{const.}$) under otherwise identical conditions is shown in orange at the bottom of Fig. 14. The temperature level for the case of lubrication failure is significantly higher than the temperature under constant oil supply. With constant oil supply, a maximum temperature of $T_{\max} = 47.14^\circ\text{C}$ is reached after 200 revolutions. A difference of $\Delta T = 13.23\text{ K}$ compared to the course of the simulation under lubrication failure.

For the investigations, the sensor TI TMP117 was modeled as virtual sensor, which will be used in the second generation of SiPB-prototypes. Compared to the TI LM73, the TMP117 offers the advantages of lower energy con-

sumption and higher measurement accuracy. The thermal mass of the plain bearing is 200,000 times greater than that of the individual temperature sensors of the SiPB. Due to the minimal thermal mass of the sensors, no influence on the thermal behavior of the plain bearing is to be expected by abstracting the temperature sensors in the simulation. By considering the response behavior of the temperature sensors used, it is possible to estimate the recorded temperature curves of the SiPB's integrated sensors. The temperature value T_S of the sensor with the thermal mass M_T , which has an initial temperature of T_I and is adjacent to an object with the surface temperature T_O via the thermal resistance R_{SO} , is calculated according to Eq. 5:

$$T_S = T_I - (T_O - T_I) \cdot e^{-\frac{t}{R_{SO} \cdot M_T}} \tag{5}$$

The thermal mass M_T of the temperature sensor is 0.0051 J/K and the thermal resistance from the top of the sensor housing to the junction is 82.3 K/W [47]. A thickness of $25\ \mu\text{m}$ [48] and a thermal conductivity of $\lambda = 2.3\text{ W/m}\cdot\text{K}$ [49] can be considered for the thermal paste applied between the bearing surface and contact area of the bearing, resulting in a thermal resistance of 2.7 K/W . The total thermal resistance therefore is $R_{SO} = 85\text{ K/W}$. The maximum temperature on the running surface of the simulation (orange line) can be compared to recorded maximum temperature of the SiPB's virtual sensors (blue line). For the two simulation cases presented in this subchapter, the

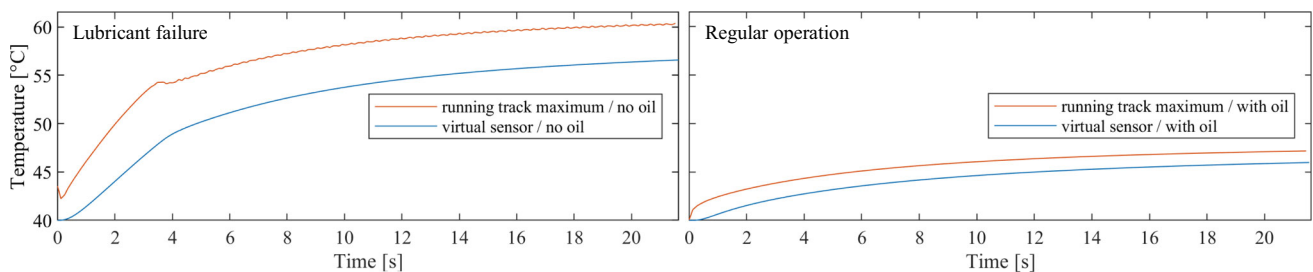


Fig. 14 Temperature curves of the maximum bearing temperature and maximum virtual sensor temperature in case of lubricant failure (top) and regular operation (bottom) ($T = 40^\circ\text{C}$; $\bar{v} = 3.5\text{ m/s}$; $\bar{p} = 5\text{ MPa}$)

curves of the maximum recorded temperature of the SiPB sensors, which are calculated with Eq. 7, are displayed in blue in Fig. 14. The differences between regular operation and lubricant failure are also clearly recognizable in the sensor temperature signal. The maximum sensor temperature $\Delta T_{S,\varphi=187.5^\circ}$ increases by 10.2°C within the first 5 s of a lubricant failure (without failure $\Delta T_{S,\varphi=210^\circ}$ increase by 2.8°C).

The investigations indicate that the SiPB is well suited for the detection of lubricant failure. The results presented have only shown operating conditions under which no immediate bearing failure is to be expected due to lubricant failure. Lubricant failure, which causes bearing failure, is accompanied by increased friction and heat input into the SiPB. The temperature field measurement therefore should be even more sensitive for detecting these critical cases. Experimental validation of the SiPB regarding the detection of lubricated supply failures is planned. The validated, simulative approach can also enable the model-based design of the sensor system (number, position and measurement frequency of the temperature sensors) for varying bearing sizes.

6 Thermoelectric Energy Harvesting and Energy Demand

In this chapter, the feasibility of thermoelectric energy harvesting using a commercially available TEG is investigated experimentally. TEGs generate electrical energy from the heat generated in the plain bearing based on thermoelectric effects. In [2], the energy requirement of the first SiPB-prototype was determined to be $P=1958\text{ mW}$ at an operating voltage of $U_{\text{operating}}=3.3\text{ V}$ ($f_M=0.2\text{ Hz}$). This is the energy demand without the implementation of optimization measures to further reduce the energy level.

The TEG MGM250-71-10-16 [50] was used for the investigations. The TEG has a width and length of 22 mm

and a thickness of 3.2 mm. Firstly, a defined temperature difference was applied to the TEG under laboratory conditions using a heating and cooling element. Simultaneously, the harvestable power and the output voltage were measured. Figure 15 illustrates the amount of energy that can be harvested as a function of the TEG's output voltage. The efficiency of a commercially available DC-DC converter to provide the necessary operating voltage $U_{\text{out},3.3\text{ V}}$ for the SiPB of $\eta=60\%$ has been considered.

A TEG output voltage of $U_{\text{out}}\approx 80\text{ mV}$ is required for continuous operation of the non-energy-demand-optimized SiPB-prototype using a single TEG. To harvest the energy needed to operate the SiPB-Prototype, a temperature difference of at least $\Delta T_{\text{TEG}}=4.2^\circ\text{C}$ must be present at the TEG. For the experimental investigations of the harvestable energy within the plain bearing, tests were conducted under constant operating conditions ($\bar{v}=\text{const.}$; $\bar{p}=\text{const.}$; $T_{\text{in}}=\text{const.}$). A test duration of 2 h was selected as the test completion criterion. At this point, the thermal equilibrium of the system has usually been reached, and the measurable output voltage of the TEG no longer significantly changes. Following a complete standstill of the shaft, these constant operating conditions represent the most disadvantageous case for thermoelectric energy harvesting, as the temperature gradient occurring at the TEG is minimal in the thermal equilibrium state. In Fig. 16 the output voltages of the TEG, which is inserted into the bearing at an angular position of $\varphi=90^\circ$ (see Fig. 5 right side), are displayed.

A comparison of the left and middle graphs in Fig. 16 indicates that the sliding speed \bar{v} has the greatest influence on the voltage output of the TEG. For the tests shown on the left at a constant sliding speed of $\bar{v}=1\text{ m/s}$, for all three oil temperature levels the voltage output is permanently above the demand-covering limit of 80 mV. A higher T_{in} -level is accompanied by a higher output voltage of the TEG under otherwise identical operating conditions, whereby the influence of the inlet oil temperature is significantly lower than the influence of the sliding speed \bar{v} . A comparison of

Fig. 15 Harvestable Power depending on the voltage output of the TEG

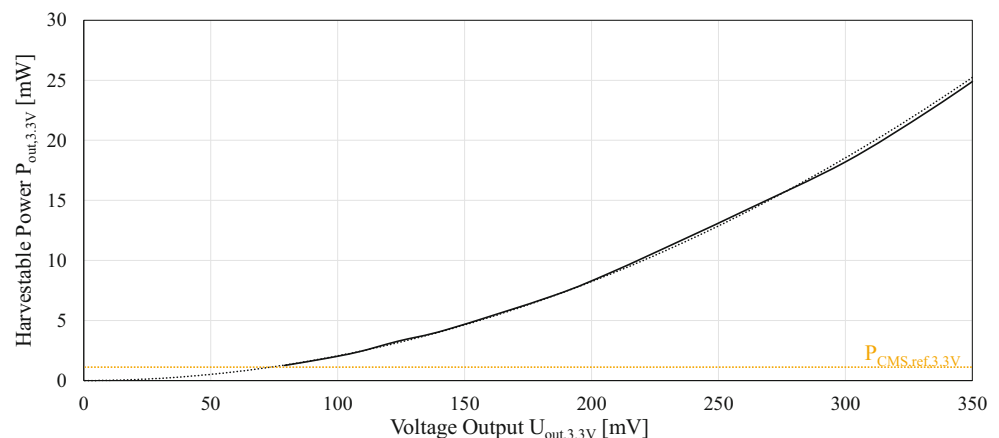


Fig. 16 Electrical voltage output TEG during test conduction

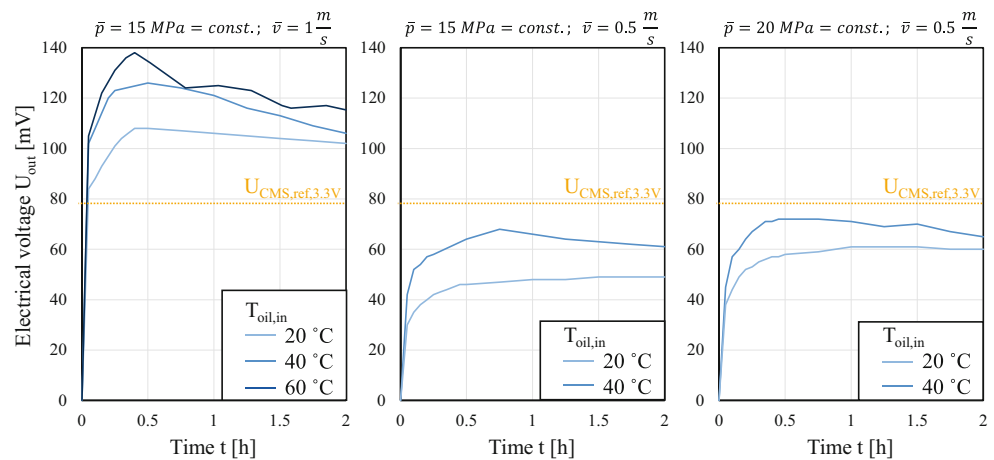


Fig. 16, center and right, shows that an increase in \bar{p} results in a slight increase in the output voltage. At a reduced sliding speed of $\bar{v}=0.5\text{ m/s}$, the output voltage at the single TEG is not sufficient to cover the non-optimized SiPB energy demand on a permanent basis.

However, rapid developments are observable in the field of energy harvesting technologies in recent years. For example, new DC/DC converters have been introduced to the market that enable the connection of several energy harvesting sources [51, 52]. By connecting the TEGs in series, the output voltage that is passed on to the DC-DC converter can be significantly increased. As a result, a multiplication of the amount of energy that can be generated can be anticipated neglecting occurring losses. Figure 5 shows that three TEGs are already integrated in the prototype under investigation and that the construction volume enables the integration of more TEGs. In future, it is planned to investigate the connection of several TEGs to the DC-DC converter.

7 Conclusion and outlook

In this paper, the investigation of a Sensor-integrating Plain Bearing (SiPB) prototype regarding the monitoring of transient operating conditions as well as lubricant failure were presented. For condition monitoring, temperature field measurement is the only suitable method for autarkic, in-situ monitoring of all damage-critical operating states of the plain bearing. In the investigations presented, the particular focus was on the suitability of the monitoring approach for highly transient operating conditions (start-stop tests) experimentally and the special event of lubricant failure simulatively. It was shown that the temperature field-based condition monitoring approach can reliably detect changes in the lubrication condition fast enough and is significantly more sensitive than the established monitoring of the oil outlet temperature. With a measuring frequency of

$f_M=0.14\text{ Hz}$, a change in the lubrication condition was detectable in 7 to 14 s for the start-stop tests. The individual start-stop cycles and associated changes in the lubrication conditions were not detectable in the oil outlet temperature, which serves as a monitoring parameter for the design of temperature safety in accordance with the DIN standard. A further improvement in the response behavior can be anticipated by increasing the measuring frequency of the SiPB. The temperature sensors used offer the possibility of operating with a maximum measuring frequency of $f_M=8.92\text{ Hz}$. The highest sampling rate possible is to be determined depending on the energy harvestable by further investigations, which are planned for the follow-up project.

Furthermore, the thermoelectrically harvestable energy budget in stationary operation was investigated in this paper. It could be shown that under stationary operating conditions, which are particularly negative with regard to the energy harvestable due to minimal temperature difference occurring at the TEG, the amount of energy that can be harvested by one TEG is in the range of the non-optimized energy demand of the SiPB-prototype.

In summary, the approaches chosen to solve the partial function of condition monitoring and energy demand coverage are promising and will be pursued for future investigations in the second funding period of the project “Auto-informative plain bearings”. To prevent imminent damage to the plain bearing, it is necessary to determine reproducible alarm limit values for failure-critical operating states, which must be quickly forwarded to the drive system’s control unit to initiate condition-based maintenance countermeasures. At the same time, the alarm limit values must be robust enough to avoid unnecessary downtimes caused by the incorrect indication of failure-critical states. To determine the alarm limit values, intensive experimental investigations are planned, in which plain bearings are operated up to the point of damage while measuring the temperature field. Once the limit values have been implemented in the SiPB’s logic, the prevention of damage will then be verified by forwarding

the alarm limit values to the test bench control system to implement countermeasures.

In the field of market-available microelectronics, rapid further development in terms of energy efficiency is to be anticipated, so that the SiPB and its microelectronic sub-components will be iteratively adapted on a regular basis to achieve complete autarky of the SiPB, the available energy budget can be increased by connecting several TEGs in series. On the other hand, to reduce the energy requirement, optimization measures can be implemented on the software side regarding demand-oriented measurement data acquisition, processing and transmission. The concept developed is highly dependent upon the thermal behavior of the plain bearing's surroundings, particularly regarding the condition monitoring and energy harvesting sub-modules. To enable the efficient transfer of the concept to other target applications and to predict accuracy and functional reliability, it is necessary to create a framework for the design of SiPBs. The MBSE methodology is ideal for developing the cyber-physical product SiPB across domains and transferring it to other target systems based on models. The aim of the second funding phase is to create a MBSE-based framework for the design of SiPB. The integration of simulative plain bearing models, as presented in this paper, will be the foundation for model-based design of SiPB for different plain bearing sizes and target systems.

Acknowledgements Funded by the Deutsche Forschungsgemeinschaft (DFG, German Research Foundation)—466775494, 441853410.

Funding Open Access funding enabled and organized by Projekt DEAL.

Conflict of interest T. Baszenski, J. Groß, K.-H. Kratz, J. Paeßens, G. Jacobs, T. Gemmeke, B. Lehmann and M. Lucassen declare that they have no competing interests.

Open Access Dieser Artikel wird unter der Creative Commons Namensnennung 4.0 International Lizenz veröffentlicht, welche die Nutzung, Vervielfältigung, Bearbeitung, Verbreitung und Wiedergabe in jeglichem Medium und Format erlaubt, sofern Sie den/die ursprünglichen Autor(en) und die Quelle ordnungsgemäß nennen, einen Link zur Creative Commons Lizenz beifügen und angeben, ob Änderungen vorgenommen wurden. Die in diesem Artikel enthaltenen Bilder und sonstiges Drittmaterial unterliegen ebenfalls der genannten Creative Commons Lizenz, sofern sich aus der Abbildungslegende nichts anderes ergibt. Sofern das betreffende Material nicht unter der genannten Creative Commons Lizenz steht und die betreffende Handlung nicht nach gesetzlichen Vorschriften erlaubt ist, ist für die oben aufgeführten Weiterverwendungen des Materials die Einwilligung des jeweiligen Rechteinhabers einzuholen. Weitere Details zur Lizenz entnehmen Sie bitte der Lizenzinformation auf <http://creativecommons.org/licenses/by/4.0/deed.de>.

References

- Hagemann T, Ding H, Radtke E et al (2021) Operating Behavior of Sliding Planet Gear Bearings for Wind Turbine Gearbox Applications—Part I: Basic Relations. *Lubricants* 9:97. <https://doi.org/10.3390/lubricants9100097>
- Paeßens J, Kratz K-H, Gemmeke T et al (2024) Design of a fully integrated sensor system of a plain bearing. *Forsch Ingenieurwes.* <https://doi.org/10.1007/s10010-024-00740-8>
- Vencl A, Rac A (2014) Diesel engine crankshaft journal bearings failures: Case study. *Eng Fail Anal* 44:217–228. <https://doi.org/10.1016/j.engfailanal.2014.05.014>
- Baszenski T, Kauth K, Kratz K-H et al (2023) Sensor integrating plain bearings: design of an energy-autonomous, temperature-based condition monitoring system. *Forsch Ingenieurwes* 87:441–452. <https://doi.org/10.1007/s10010-023-00642-1>
- Vorwerk-Handing G, Gwosch T, Schork S et al (2020) Classification and examples of next generation machine elements. *Forsch Ingenieurwes* 84:21–32. <https://doi.org/10.1007/s10010-019-00382-1>
- Kirchner E, Martin G, Vogel S (2018) Sensor Integrating Machine Elements—Key to In-Situ Measurements in Mechanical Engineering. In: Conference: 23rd International Seminar on High Technology. In, Piracicaba, Brazil
- Kirchner E, Wallmersperger T, Gwosch T et al (2024) A Review on Sensor-Integrating Machine Elements. *Adv Sens Res.* <https://doi.org/10.1002/adsr.202300113>
- Küchenhof J, Breimann R, Kirchner E et al (2024) Development of a model-based modular building kit for sensor-integrating machine elements—Theory and application. *Forsch Ingenieurwes.* <https://doi.org/10.1007/s10010-024-00761-3>
- Marheineke J, Jacobs G, Gutierrez Guzman F et al (2022) Auto-informative Gleitlager – Konzept einer autarken, temperaturbasierten Zustandsüberwachung. In: Schlecht (ed) *Dresdner Maschinenelemente Kolloquium DMK 2022*, pp 109–126 (In:)
- Deutsches Institut für Normung e. V. (2017) Gleitlager – Hydrodynamische Radial-Gleitlager im stationären Betrieb: Teil 1: Berechnung von Kreiszyylinderlagern(31652-1)
- Deutsches Institut für Normung e. V. (2017) Gleitlager – Hydrodynamische Radial-Gleitlager im stationären Betrieb: Teil 2: Funktionen für die Berechnung von Kreiszyylinderlagern(31652-2)
- VDI/VDE (1992) *Auslegung von Gleitlagerungen(2204)*
- Deutsches Institut für Normung e. V. (2017) Gleitlager – Hydrodynamische Radial-Gleitlager im stationären Betrieb: Teil 3: Betriebsrichtwerte für die Berechnung von Kreiszyylinderlagern(31652-3)
- Reynolds O (1886) On the theory of lubrication and its application to Mr. Beauchamp tower's experiments, including an experimental determination of the viscosity of olive oil. *Phil Trans R Soc* 177:157–234. <https://doi.org/10.1098/rstl.1886.0005>
- DIN e. V. (2017) Gleitlager – Hydrodynamische Radial-Gleitlager im stationären Betrieb(31652)
- Meier V, Illner T (2013) Gleitlagerverschleißgrenzen – Einsatzgrenzen von hydrodynamischen Weißmetallgleitlagern infolge von Verschleiß. Frankfurt
- König F, Sous C, Jacobs G (2021) Numerical prediction of the frictional losses in sliding bearings during start-stop operation. *Friction* 9:583–597. <https://doi.org/10.1007/s40544-020-0417-9>
- Lucassen M, Decker T, Guzmán FG et al (2023) Simulation methodology for the identification of critical operating conditions of planetary journal bearings in wind turbines. *Forsch Ingenieurwes* 87:147–157. <https://doi.org/10.1007/s10010-023-00626-1>
- Xu F, Ding N, Li N et al (2023) A review of bearing failure Modes, mechanisms and causes. *Eng Fail Anal* 152:107518. <https://doi.org/10.1016/j.engfailanal.2023.107518>
- Peterka P, Krešák J, Vojtko M et al (2020) Failure analysis of the journal bearing pulley of the cargo cable way. *Eng Fail Anal* 111:104329. <https://doi.org/10.1016/j.engfailanal.2019.104329>
- Yin F, Lu W, Nie S et al (2021) Failure analysis and improvement of the tribological performance of sliding bearing tribopair

- in integrated energy recovery-pressure boost device. *Ceram Int* 47:30367–30380. <https://doi.org/10.1016/j.ceramint.2021.07.217>
22. Czichos H, Habig K-H (2010) *Tribologie-Handbuch. Vieweg+Teubner, Wiesbaden*
 23. Mokhtari Molk Abadi N (2020) *Überwachung hydrodynamischer Gleitlager basierend auf der Körperschallanalyse. Dissertation, TU Berlin*
 24. Hossain MI, Zahid MS, Chowdhury MA et al (2023) MEMS-based energy harvesting devices for low-power applications—a review. *Results Eng* 19:101264. <https://doi.org/10.1016/j.rineng.2023.101264>
 25. Sezer N, Koç M (2021) A comprehensive review on the state-of-the-art of piezoelectric energy harvesting. *Nano Energy* 80:105567. <https://doi.org/10.1016/j.nanoen.2020.105567>
 26. Ibn-Mohammed T, Koh S, Reaney IM et al (2017) Perovskite solar cells: An integrated hybrid lifecycle assessment and review in comparison with other photovoltaic technologies. *Renew Sustain Energy Rev* 80:1321–1344. <https://doi.org/10.1016/j.rser.2017.05.095>
 27. Slabov V, Kopyl S, Soares Dos SMP et al (2020) Natural and Eco-Friendly Materials for Triboelectric Energy. *Harvest Nanomicro Lett* 12:42. <https://doi.org/10.1007/s40820-020-0373-y>
 28. Miao G, Fang S, Wang S et al (2022) A low-frequency rotational electromagnetic energy harvester using a magnetic plucking mechanism. *Appl Energy* 305:117838. <https://doi.org/10.1016/j.apenergy.2021.117838>
 29. Junior AOH, Maran A, Henao NC (2018) A review of the development and applications of thermoelectric microgenerators for energy harvesting. *Renew Sustain Energy Rev* 91:376–393. <https://doi.org/10.1016/j.rser.2018.03.052>
 30. Jiang L, Yang Y, Chen Y et al (2020) Ultrasound-Induced Wireless Energy Harvesting: From Materials Strategies to Functional Applications. *Nano Energy*. <https://doi.org/10.1016/j.nanoen.2020.105131>
 31. Muscat A, Bhattacharya S, Zhu Y (2022) Electromagnetic Vibrational Energy Harvesters: A Review. In: *Sensors*, vol 22. Basel, <https://doi.org/10.3390/s22155555>
 32. Niu X, Yu J, Wang S (2009) Experimental study on low-temperature waste heat thermoelectric generator. *J Power Sources* 188:621–626. <https://doi.org/10.1016/j.jpowsour.2008.12.067>
 33. Gou X, Xiao H, Yang S (2010) Modeling, experimental study and optimization on low-temperature waste heat thermoelectric generator system. *Appl Energy* 87:3131–3136. <https://doi.org/10.1016/j.apenergy.2010.02.013>
 34. Snyder GJ, Toberer ES (2008) Complex thermoelectric materials. *Nat Mater* 7:105–114. <https://doi.org/10.1038/nmat2090>
 35. Rowe DM (2018) *CRC Handbook of Thermoelectrics*. CRC Press
 36. Höglblom O, Andersson R (2014) Analysis of Thermoelectric Generator Performance by Use of Simulations and Experiments. *J Elec Materi* 43:2247–2254. <https://doi.org/10.1007/s11664-014-3020-x>
 37. Spies P, Pollak M, Rohmer G (2008) Power Management for Energy Harvesting Applications. *Proc 1st Int Workshop Power Supply Chip (pwrsoc)* 08:
 38. Stojcev MK, Kosanovic MR, Golubovic LR (2009) (102009) Power management and energy harvesting techniques for wireless sensor nodes. In: *9th International Conference on Telecommunication in Modern Satellite, Cable, and Broadcasting Services*. IEEE, pp 65–72
 39. Mateu L, Codrea C, Lucas N et al (2006) Energy harvesting for wireless communication systems using thermo generators. In: *Proc. of the XXI Conference on Design of Circuits and Integrated Systems (DCIS)*
 40. Sudevalayam S, Kulkarni P (2011) Energy Harvesting Sensor Nodes: Survey and Implications. *Ieee Commun Surv Tutor* 13:443–461. <https://doi.org/10.1109/SURV.2011.060710.00094>
 41. Kumaravel V, Bartlett J, Pillai SC (2021) Solid Electrolytes for High-Temperature Stable Batteries and Supercapacitors. *Adv Energy Mater*. <https://doi.org/10.1002/aenm.202002869>
 42. Gupta BB, Perez GM, Agrawal DP et al (2020) *Handbook of Computer Networks and Cyber Security*. Springer, Cham
 43. Jondhale SR, Maheswar R, Lloret J (2022) Fundamentals of Wireless Sensor Networks. In: Jondhale SR, Maheswar R, Lloret J (eds) *Received Signal Strength Based Target Localization and Tracking Using Wireless Sensor Networks*. Springer, Cham, pp 1–19
 44. (2015) https://www.ti.com/lit/ds/symlink/lm73.pdf?ts=1740043635415&ref_url=https%253A%252F%252Fwww.ti.com%252Fproduct%252Fde-de%252FLM73. Accessed 2020
 45. Marheineke J (2024) *Ermittlung und Bewertung des Verhaltens von hydrodynamischen Gleitlagern bei Mangelschmierung*. Dissertation, RWTH Aachen University
 46. Schopf E, Steeg M (1982) *Untersuchung des Verhaltens von Gleitlagerwerkstoffen bei Störung des hydrodynamischen Betriebs*. In: Bunk W, Hansen J, Geyer M (eds) *Gleitlager · Wellendichtungen*. Springer Berlin Heidelberg, Berlin, Heidelberg, pp 271–317
 47. (2018) https://www.ti.com/lit/ds/symlink/tmp117.pdf?ts=1740392415609&ref_url=https%253A%252F%252Fwww.ti.com%252Fproduct%252Fde-de%252FTMP117. Accessed 2024
 48. Leong C-K, Chung D (2004) Carbon black dispersions and carbon–silver combinations as thermal pastes that surpass commercial silver and ceramic pastes in providing high thermal contact conductance. *Carbon* 42:2323–2327. <https://doi.org/10.1016/j.carbon.2004.05.013>
 49. (2024) [https://www.fischerelektronik.de/web_fischer/de_DE/K%C3%BChlk%C3%B6rper/E01.08/W%C3%A4rmeleitpasten%20und%20W%C3%A4rmeleitfilm/\\$catalogue/fischerData/PR/WLPF23_10/search.xhtml](https://www.fischerelektronik.de/web_fischer/de_DE/K%C3%BChlk%C3%B6rper/E01.08/W%C3%A4rmeleitpasten%20und%20W%C3%A4rmeleitfilm/$catalogue/fischerData/PR/WLPF23_10/search.xhtml). Accessed 2020
 50. (2017) <https://docs.rs-online.com/9c51/0900766b8163f4f0.pdf>. Accessed 2020
 51. Kumar L, Jain S (2013) A multiple source DC/DC converter topology. *Int J Electr Power Energy Syst* 51:278–291. <https://doi.org/10.1016/j.ijepes.2013.02.020>
 52. Singh AR, Suresh K, Parimalasundar E et al (2024) Design and performance evaluation of a multi-load and multi-source DC-DC converter for efficient electric vehicle power systems. *Sci Rep* 14:25718. <https://doi.org/10.1038/s41598-024-77349-y>

Publisher's Note Springer Nature remains neutral with regard to jurisdictional claims in published maps and institutional affiliations.